

Article

Crystal Structure and Hirshfeld Surface Analysis of Bis(Triethanolamine)Nickel(II) Dinitrate Complex and a Revelation of Its Characteristics via Spectroscopic, Electrochemical and DFT Studies Towards a Promising Precursor for Metal Oxides Synthesis

Wanchai Deelod^{1,†} , Suttipong Wannapaiboon^{2,†} , Pimporn Pansiri³, Pornsawan Kumpeerakij³, Khamphree Phomphrai⁴, Apirat Laobuthee³, Yuranan Hanlumyung³, Songwut Suramitr¹, Piyanut Pinyou^{5,*} , and Worawat Wattanathana^{3,*} 

¹ Department of Chemistry, Faculty of Science, Kasetsart University, Ladyao, Chatuchak, Bangkok 10900, Thailand; wanchai.de@ku.th (W.D.); fsciswsm@ku.ac.th (S.S.)

² Synchrotron Light Research Institute, 111 University Avenue, Suranaree, Muang, Nakhon Ratchasima 30000, Thailand; suttipong@slri.or.th

³ Department of Materials Engineering, Faculty of Engineering, Kasetsart University, Ladyao, Chatuchak, Bangkok 10900, Thailand; pimporn.pans@ku.th (P.P.); pornsawan.ku@ku.th (P.K.); fengapl@ku.ac.th (A.L.); yuranan.h@ku.th (Y.H.)

⁴ Department of Materials Science and Engineering, School of Molecular Science and Engineering, Vidyasirimedhi Institute of Science and Technology, Rayong 21210, Thailand; khamphree.p@vistec.ac.th

⁵ School of Chemistry, Institute of Science, Suranaree University of Technology, 111 University Avenue, Suranaree, Muang, Nakhon Ratchasima 30000, Thailand

* Correspondence: piyanutp@sut.ac.th (P.P.); fengwwa@ku.ac.th (W.W.)

† The authors shared co-first authorship.

Received: 6 May 2020; Accepted: 28 May 2020; Published: 3 June 2020



Abstract: Metal complexes with chelating ligands are known as promising precursors for the synthesis of targeted metal oxides via thermal decomposition pathways. Triethanolamine (TEA) is a versatile ligand possessing a variety of coordination modes to metal ions. Understanding the crystal structure is beneficial for the rational design of the metal complex precursors. Herein, a bis(triethanolamine)nickel (II) dinitrate (named as Ni-TEA) crystal was synthesized and thoroughly investigated. X-ray crystallography revealed that Ni(II) ions adopt a distorted octahedral geometry surrounded by two neutral TEA ligands via two N and four O coordinates. Hirshfeld surface analysis indicated the major contribution of the intermolecular hydrogen-bonding between —OH groups of TEA in the crystal packing. Moreover, several O—H stretching peaks in Fourier transformed infrared spectroscopy (FTIR) spectra emphasizes the various chemical environments of —OH groups due to the formation of the hydrogen-bonding framework. The Density-functional theory (DFT) calculation revealed the electronic properties of the crystal. Furthermore, the Ni-TEA complex is presumably useful for metal oxide synthesis via thermal decomposition at a moderate temperature (380 °C). Cyclic voltammetry indicated the possible oxidative reaction of the Ni-TEA complex at a lower potential than nickel(II) nitrate and TEA ligand, highlighting its promising utility for the synthesis of mixed valence oxides such as spinel structures.

Keywords: metal complex; triethanolamine; coordination chemistry; crystal structure; hydrogen bonding; Hirshfeld surface analysis; X-ray diffraction.

1. Introduction

Metal complexes with chelating ligands are well-known as one of the molecular single-source precursors (SSPs) used for the synthesis of targeted metal oxides, including single-phase, stoichiometric-mixed and hetero-metal-doped metal oxides via thermal decomposition pathways. [1–3] Controlled incorporation of the targeted metals into the metal complexes provides a way to define the stoichiometry at the molecular level and to precisely control the distribution of targeted metals in the material matrix [4–6]. Pre-formed Metal-O bonds in the complex precursors possibly enhance nucleation by lowering the energy barrier and reducing the diffusion distances required to assemble the solid-state structures [4,7]. Moreover, the heat released during the decomposition of the chelating organic ligands can also facilitate the crystallization process [8]. As a result, the targeted metal oxides can be obtained at a lower temperature, which provides a better chance to manipulate their particle sizes and surface areas in order to achieve the desired properties [7,8]. Hence, understanding crystal structures and characteristic features of the metal complex precursors is a crucial step that allows for fine tuning of the properties of the complex-derived oxide materials.

Triethanolamine (TEA) is widely known as a versatile ligand possessing three hydroxyethyl groups and one nitrogen donor atom. TEA can coordinate as tridentate and/or tetradentate ligands, and one or two TEA molecules per metal ion center can be found in metal-TEA complexes. Hence, a variety of TEA-chelating complex structures is observed depending on the central metal ions and the synthetic parameters [9–23]. In cases of tetradentate ($\kappa 4\text{-N,O,O',O''}$) coordination, a metal ion coordinates to a TEA ligand to form the atrane structure [11–13], or to two tetradentate TEA ligands to form 8-coordinated metal complexes [14,15]. In cases of the tridentate ($\kappa 3\text{-N,O,O'}$) coordination, a metal ion generally coordinates with two tridentate TEA ligands to form the 6-coordinated metal complexes [16–22]. The mixed tridentate and tetradentate TEA ligands are also observed exhibiting the 7-coordinated metal complex [23]. Moreover, the diverse structural feature of metal-TEA complexes can be attributed to the deprotonation of the ethanolic protons while coordinating with metals. For example, different levels of deprotonation at TEA ligand in the Cu-TEA-1,2-di(4-pyridyl) ethylene complex leads to different coordination modes [24]. Thereby, in-depth study of crystal structures and characteristic features of the metal-TEA complexes is essential for further use in the desired applications.

Metal-TEA complexes exhibit various applications, including catalysis, gas captures, bioactive pharmacochemical compounds and promising precursors for the synthesis of metal oxide materials. Specifically, metal-TEA complexes can be used as highly selective catalysts for the oxidation of alkanes [25] and of alkylarenes to phenyl ketones under mild conditions [26]. It also shows the catalytic performance in the reduction of CO₂ to produce formate. [27] As a capturing agent, metal-TEA complexes can be applied for CO₂ capture by employing the CO₂ insertion mechanism [28,29]. Furthermore, metal-TEA compounds are also biologically active. As an ancillary ligand, TEA in mixed-ligand metal complexes enhances the physiological action of bioactive substances [12]. In vitro pharmacochemical study of the Cu-TEA complexes indicates antioxidant activity due to the scavenging property towards superoxide anion radicals. [30] Furthermore, metal-TEA complexes were directly used as precursors for the preparation of single-phase and mixed metal oxides by employing thermal decomposition without requiring a prior sol-gel formation [31,32]. The thermal decomposition of metal-TEA complexes provides various advantages such as a straightforward synthesis procedure to achieve the desired metal oxides with controlled compositions, low cost due to high commercial availability of TEA and a possibility for up-scale production. Moreover, variability of complex formation of TEA with miscellaneous cations has revealed many successful preparations of oxide materials [33–40].

In this work, a complex between nickel(II) nitrate hexahydrate and TEA ligand, so-called the bis(triethanolamine)nickel(II) dinitrate (Ni-TEA) complex, was synthesized. Even though the crystallographic data and the basic physical properties of the obtained Ni-TEA complex have been revealed previously by Levy et al. [41] and Rasmussen et al. [42], the intermolecular interactions and hydrogen bonding structure within the crystal remains unexplored. Herein, the structural information

and the hydrogen bonding framework of the obtained Ni-TEA crystal was derived from single-crystal X-ray diffraction and Hirshfeld surface analysis. This understanding would be beneficial to correlate the crystallographic information with the observed properties. Moreover, the corresponding characteristic features were thoroughly investigated by employing spectroscopic, electrochemical and quantum chemical studies. The quantum chemical calculation was performed to examine the frontier molecular orbitals and electronic transitions between the highest occupied molecular orbital (HOMO) and the lowest unoccupied molecular orbital (LUMO) to predict the electronic absorption spectra. Fourier transformed infrared spectroscopy (FTIR) and powder X-ray diffraction (PXRD) were carried out to confirm the formation of hydrogen-bonding framework in the crystal and the homogeneity of the obtained product, respectively. In order to clarify the promising potential of the Ni-TEA complex for use as a precursor for the synthesis of metal oxides via thermal decomposition, thermal gravimetric analysis (TGA) was employed. A comparison of the electrochemical behavior between the Ni-TEA complex and the corresponding ethanolic solutions of precursors ($\text{Ni}(\text{NO}_3)_2 \cdot 6\text{H}_2\text{O}$ and TEA) by performing the cyclic voltammetry (CV) could indicate the redox potential of the complex. Additionally, the possibility to produce such mixed-valence oxides by using the Ni-TEA complex as an SSP is discussed.

2. Materials and Methods

2.1. Synthesis and Crystallization of the Ni-TEA Complex

Analytical grade chemicals, namely nickel(II) nitrate hexahydrate ($\text{Ni}(\text{NO}_3)_2 \cdot 6\text{H}_2\text{O}$, UNIVAR Ajax Finechem, Thermo-Fisher scientific), ethanol and TEA ($(\text{OHCH}_2\text{CH}_3)_3\text{N}$, KEMAUS, Australia), were used for material synthesis. An ethanolic solution of $\text{Ni}(\text{NO}_3)_2 \cdot 6\text{H}_2\text{O}$ was prepared by dissolving 60 mmol of $\text{Ni}(\text{NO}_3)_2 \cdot 6\text{H}_2\text{O}$ in 30 mL ethanol. Then, 120 mmol of TEA was separately dissolved in 30 mL ethanol. The TEA solution was added dropwise into the $\text{Ni}(\text{NO}_3)_2 \cdot 6\text{H}_2\text{O}$ solution; meanwhile, the mixture was continually stirred at room temperature. After that, the mixtures were refluxed at 85 °C for an hour and then cooled down naturally. The Ni-TEA complex was subsequently crystallized after the reaction mixture was left at room temperature overnight. The appearance of the Ni-TEA complex was the blue needle-shaped crystals. The Ni-TEA crystals were filtered out and rinsed with an excess amount of ethanol before being dried overnight in a hot air oven (at a constant temperature of 60 °C). The dried crystals were kept in a desiccator prior to further characterization.

2.2. Single-Crystal X-Ray Diffraction

A single crystal (with suitable quality for single-crystal X-ray diffraction (SC-XRD)) of the prepared Ni-TEA complex was selected under an optical microscope. X-ray crystallographic data of the Ni-TEA complex were collected at 298 K on a Bruker D8 venture (Bruker AXS GmbH, Karlsruhe, Germany) using Photon II detector and $\text{I}\mu\text{S}$ 3.0 Microfocus source, Mo $\text{K}\alpha$ radiation ($\lambda = 0.71073 \text{ \AA}$). Cell refinement and data reduction were carried out by SAINT [43]. Absorption correction was done by the multi-scan method using SADABS [44]. Using Olex2 [45], the structure was solved with the ShelXT [46] structure solution program using intrinsic phasing and refined with the ShelXL [47] refinement package using a least squares minimization. All non-hydrogen atoms were treated anisotropically. The O-bonded H atoms (H1, H2 and H3) that are responsible for the hydrogen bonding framework were located in a difference Fourier map and were freely refined. The other hydrogen atoms were refined using a riding model with $d(\text{C}-\text{H}) = 0.99 \text{ \AA}$ and $U_{\text{iso}}(\text{H}) = 1.2U_{\text{eq}}(\text{C})$ for $-\text{CH}_2-$ hydrogen atoms. The Mercury software package [48] was used to prepare molecular graphics and materials for publication. The summary of the crystallographic data for the Ni-TEA complex is given in Table 1.

Table 1. Crystal data and structure refinement details for bis(triethanolamine)nickel(II) dinitrate complex (Ni-TEA complex).

Crystallographic Data and Structural Refinement Details	Bis(triethanolamine)Nickel(II) Dinitrate
Empirical formula	C ₁₂ H ₃₀ N ₄ O ₁₂ Ni
Formula weight	481.11
Temperature/K	293.15
Crystal system	Monoclinic
Space group	P2 ₁ /c
a/Å	7.224(3)
b/Å	14.777(6)
c/Å	9.173(4)
α/°	90
β/°	93.198(18)
γ/°	90
Volume/Å ³	977.7(7)
Z	2
ρ _{calc} /cm ³	1.634
μ/mm ⁻¹	1.063
F(000)	508.0
Crystal size/mm ³	0.394 × 0.267 × 0.202
Radiation	Mo Kα (λ = 0.71073)
2θ range for data collection/°	5.232 to 61.27
Index ranges	-10 ≤ h ≤ 10, -21 ≤ k ≤ 21, -13 ≤ l ≤ 13
Reflections collected	88,417
Independent reflections	3016 [R _{int} = 0.0262, R _{sigma} = 0.0083]
Data/restraints/parameters	3016/0/143
Goodness of fit on F ²	1.074
Final R indexes [I ≥ 2σ (I)]	R ₁ = 0.0221, wR ₂ = 0.0574
Final R indexes [all data]	R ₁ = 0.0226, wR ₂ = 0.0577
Largest difference peak/hole /e Å ⁻³	0.51/-0.53

2.3. Characterization of the Ni-TEA Complex

Chemical functional groups of the prepared Ni-TEA complex were investigated by Fourier-transform infrared (FTIR) spectroscopy. The FTIR spectrum was recorded by using the Fourier-Transform infrared spectrophotometer (Bruker, Alpha FT-IR spectrometer, Hong Kong) in the range of 4000–375 cm⁻¹ with a spectral resolution of 2 cm⁻¹. The Ni-TEA crystals were finely ground together with KBr and then uniaxially pressed into a pellet before performing the FTIR measurement. The UV-VIS spectrum of the Ni-TEA complex in the ethanolic solution with a concentration of 1 × 10⁻⁵ M was measured using a UV/VIS/NIR spectrophotometer (JASCO V-670, Japan).

Powder X-ray diffraction (XRD) was performed at ambient temperature at Beamline 1.1W (Multiple X-ray Techniques) at Synchrotron Light Research Institute, Thailand, using the monochromatic synchrotron X-ray radiation of the energy 12 keV (wavelength of 1.0332 Å). The powder sample was packed in Kapton capillary with a diameter of 0.5 mm and then aligned using a goniometer head. It should be noted that the capillary was constantly rotated during the powder XRD measurement. The diffraction pattern was recorded by a strip detector (Mythen6K 450, Dectris®) in the 2θ range of 5°–35° (with respect to the X-ray energy of 12 keV). The observed XRD pattern was compared to the calculated XRD pattern generated by the SC-XRD data using Mercury software [48].

Moreover, elemental composition of the Ni-TEA complex was analyzed by wavelength dispersive X-ray fluorescence (WD-XRF, Rigaku ZSX Primus IV, Rh anode X-ray generator, combined detector so-called Scintillation Counter for heavy elements and Flow Proportional Counter for light elements). The decomposition behavior of the Ni-TEA complex was determined by thermogravimetric analysis (TGA, Perkin Elmer TGA analyzer). The Ni-TEA complex was loaded into an alumina crucible and then heated from 50–400 °C using a heating rate of 7 °C/min under the flow of air zero (flow rate of 100 cm³/min).

2.4. Computational Calculation

The calculations were performed within the density functional theory and its time-dependent counterpart (DFT and TD-DFT). This level of calculation has yielded reliable results for the prediction of electronic spectra of chromospheres at a relatively low computational cost, and it is one of the most popular methods used for the evaluation of excitation energies [49,50]. The ground state and the first active singlet state structures of the Ni-TEA complex were optimized at the PBE0/6-311G(d,p) [51–53] level of the theory using Gaussian 09 [54]. Vertical excitation energies for 10 low-lying excited states were calculated. To determine the solvent effect (ethanol, $\epsilon = 24.3$), the approximation by polarizable continuum method (PCM) was used [55,56].

2.5. Electrochemical Study of the Ni-TEA Complex

Cyclic voltammetry was performed with an EmStat blue plus potentiostat (PalmSens, Houten, The Netherlands). A conventional three-electrode system including a glassy carbon working electrode (diameter 3 mm), a Pt wire as a counter electrode and an Ag/Ag⁺ (0.01 M AgNO₃) reference electrode, was used for the electrochemical study. Each ethanolic solution was purged with argon for 15 min prior to the experiment. The measurements were carried out under argon atmosphere in the ethanol solvent containing 0.1 M LiClO₄ (Sigma Aldrich, St. Louis, MO, USA) as a supporting electrolyte. Since the measurements were conducted in ethanolic solution, the perchlorate salt was used herein in order to achieve complete dissolving and consequently yield a reasonably high conductivity. Note that we carefully handled the perchlorate electrolyte during the experiment by avoiding the high temperature reaction and high current density and voltage that could lead to violent oxidative reactions.

3. Results and Discussion

3.1. Crystal Structure

The ORTEP plot showing the complete molecular structure with 50% probability level and its numbering scheme is illustrated in Figure 1. The asymmetric unit of the title compound contains one-half of the molecule of the bis(triethanolamine- κ^3 -N,O,O')nickel(II) complex and a nitrate counter ion. The other half was generated by inversion symmetry. Therefore, the complete titled molecule consists of a nickel(II) ion datively-bonded with two tridentate TEA ligands in the inner coordination sphere and two nitrate anions in the outer coordination sphere. The overall charge of the bis(triethanolamine- κ^3 -N,O,O')nickel(II) complex is 2+ as the TEA ligands coordinated by their neutral form. To maintain the charge neutrality, a unit cell of the titled compound consists of two complex cations and four nitrate counter anions. According to the coordination with two tridentate and chelating TEA ligands, the nickel(II) central ions adopt the distorted octahedral geometry in the NiN₂O₄ coordination environment as a similar geometry in the complex with sulfate anion reported previously [22]. Moreover, a six-coordinate Ni(II) ion was also observed for the Ni-based complex of TEA with chloride [57], saccharine [17], acetate [16] and squarate [58]. According to the inversion symmetry, the two nitrogen atoms are in trans-conformation with respect to each other, resulting in the linear N1-Ni-N1¹ bond angle. Moreover, the O1-Ni-O1¹ and O2-Ni-O2¹ bond angles are also 180°. The Ni-O1 bonds (2.0519(8) Å) are a bit shorter than the Ni-O2 bonds (2.0751(9) Å) due to the different hydrogen bond formation. The Ni-N1 bond is longer (2.1020(10) Å) than both the Ni-O bonds due to the larger atomic radius of N than O. The N–Ni–O bond angles are in the range of 80.81(4)° to 99.19(4)°, confirming the distorted octahedral shaped complex.

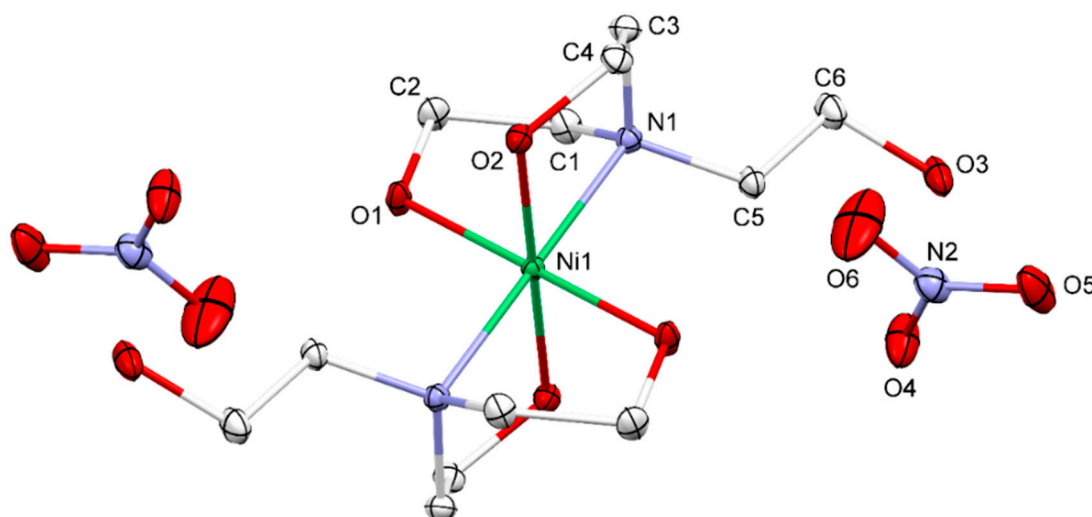


Figure 1. Molecular structures of the Ni-TEA complex with principal atom labels.

The geometry of the $[\text{Ni}(\text{TEA})_2]^{2+}$ coordination sphere in the complex has resembled the endo and exo conformation of the triethanolammonium cations with organic anions [59]. The endo and exo conformation is the TEA structure, in which one hydroxyethyl moiety (exo branch) is rotated around the N–C bond, creating the infinite chain of TEA [59].

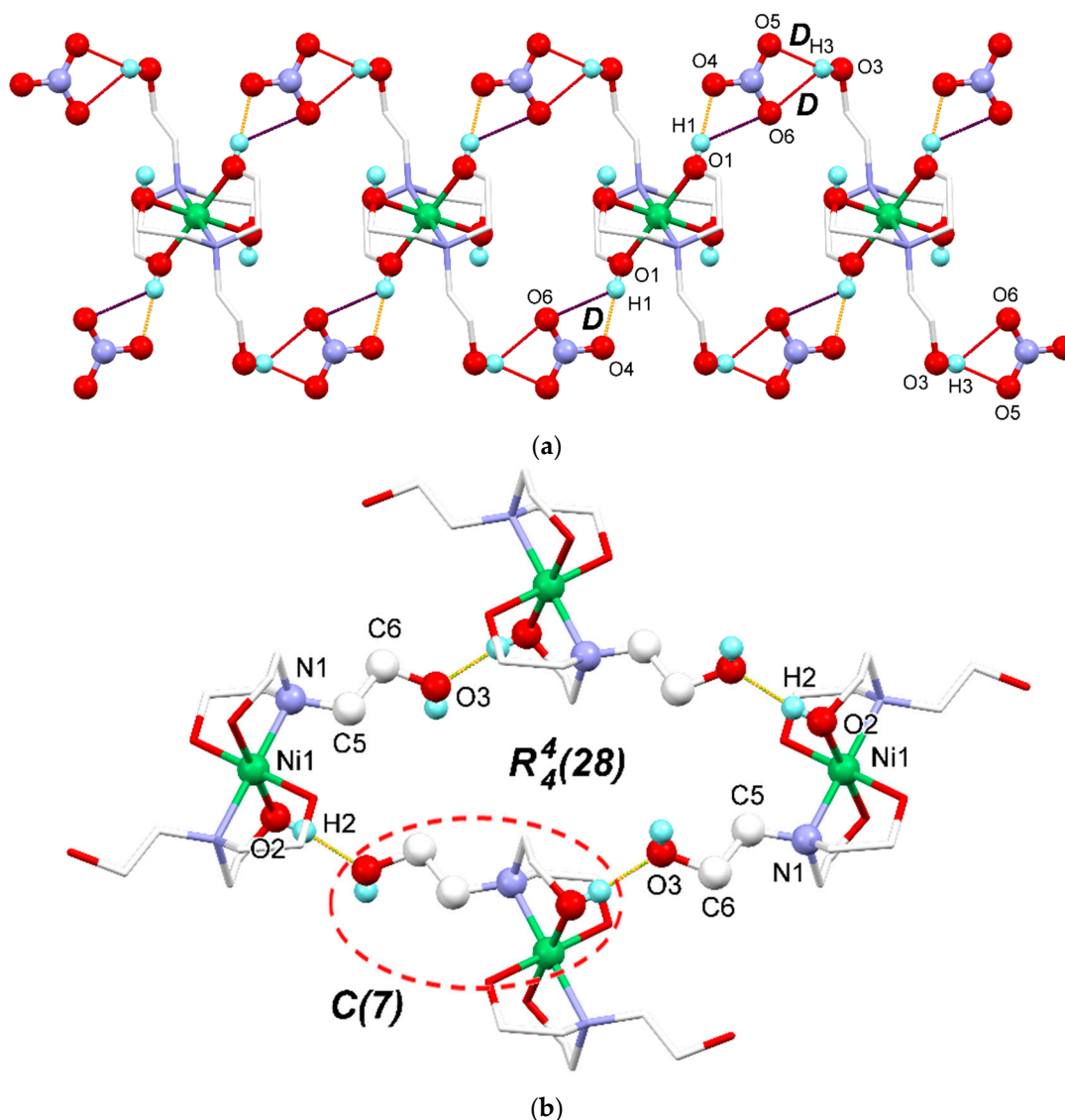
3.2. Supramolecular Features

In the crystal structure, classical intermolecular O–H \cdots O hydrogen bonds were observed (Table 2), which link the Ni-TEA complex and nitrate ions together. The O–H groups in the complex cations and nitrate anions are involved in the construction of a two-dimensional hydrogen-bonded network (Figure 2). For detailed analysis of the hydrogen bonding framework, the graph set notation is used to describe the different types of hydrogen bonds observed within the crystal structure of the Ni-TEA complex [60–62]. The uncoordinated O–H group (O3–H3) can set up two discrete hydrogen bonds with the graph set of *D* to two oxygen atoms in the NO_3^- anion (O3–H3 \cdots O5 and O3–H3 \cdots O6) (Figure 2a shown by red lines and Table 2). The hydrogen acceptor (H–A) distances are in the range from 2.21(2)–2.30(2) Å. One of the coordinated O–H groups (O1–H1) can also link to the oxygen atom of the nitrate anion (O4) by a discrete hydrogen bond (*D* graph set) with a relatively shorter H–A distance (1.86(2) Å) than those of O3–H3 \cdots O5 and O3–H3 \cdots O6 interactions. However, the O6 atom is located too far for the hydrogen bond with H1 to be formed. Apart from the discrete hydrogen bonds, the other coordinated OH groups (O2–H2) can create the hydrogen bonding chain with *C*(7) graph set linking between different complex cations via O2–H2 \cdots O3 by the O3–C6–C5–N1–Ni1–O2–H2 synthon (Figure 2b) with an H–A distance of 1.843(18) Å. In this case, O3 acts as a hydrogen bond acceptor only. The same synthon can join four units of the complex cations together giving rise to the $R_4^4(28)$ hydrogen bond ring comprising of 4 H-bond donors, 4 H-bond acceptors, and 28 atoms in the ring (Figure 2b). Moreover, the larger ring size with the $R_6^6(42)$ graph set is also found when hydrogen bonds assemble seven units of the complex cations together. The formation of the hydrogen bonding framework stabilizes the crystal structure of the Ni-TEA complex.

Table 2. Hydrogen bonds in the crystal structure of the bis(triethanolamine)nickel(II) dinitrate (Ni-TEA) complex.

D-H...A	d(D-H)/Å	d(H-A)/Å	d(D-A)/Å	D-H-A/°
O2-H2...O3 ^a	0.801(18)	1.843(18)	2.6412(13)	173.5(17)
O1-H1...O4	0.82(2)	1.86(2)	2.6689(14)	168(2)
O3-H3...O5 ^b	0.78(2)	2.21(2)	2.9533(15)	161(2)
O3-H3...O6 ^b	0.78(2)	2.30(2)	2.9535(16)	142.1(19)

$$^a 1-X, 1/2+Y, 3/2-Z; ^b -X, 1-Y, 1-Z$$

**Figure 2.** Crystal packing of the Ni-TEA complex showing (a) discrete hydrogen bonds (D), O1-H1...O4, O3-H3...O5, and O3-H3...O6, viewing along the [001] axis, (b) O2-H2...O3 hydrogen bonding chain with the C(7) graph set and the hydrogen bonding ring with the R₄⁴(28) graph set, viewing along the [100] axis. The different colors show the hydrogen bonds with different distances where yellow, red and blue represent short, middle and long interactions, respectively.

3.3. Hirshfeld Surface Analysis

To visualize the interactions within the crystal of the Ni-TEA complex, a Hirshfeld surface (HS) analysis [63,64] was performed using Crystal Explorer 17.5 software [65]. The full fingerprint plot and those delineated into H...O/O...H, H...H, and H...N/N...H interactions are illustrated

in Figure 3a–d, respectively. Hirshfeld surfaces corresponding to the $H\cdots O/O\cdots H$, $H\cdots H$, and $H\cdots N/N\cdots H$ interactions are displayed in Figure 3e–g. The analysis of the fingerprint plot reveals that the significant interactions which contributed to the crystal packing within the Ni-TEA complex were $H\cdots O/O\cdots H$ (51.1%), $H\cdots H$ (46.6%) and $H\cdots N/N\cdots H$ (2.1%) [66]. The $H\cdots H$ contacts are characterized by a single spike at $d_e + d_i \approx 2.4 \text{ \AA}$, while the $H\cdots O/O\cdots H$ contacts are viewed as a pair of spikes at $d_e + d_i \approx 1.65 \text{ \AA}$. These results imply that the primary interaction between the packed complex cations and the nitrate anions in the crystal are the hydrogen bonds. This result agrees with the analysis of hydrogen bonding (Table 2). Other interactive contacts apart from those mentioned above have a negligible effect on the crystal packing since their total contribution is only 0.2%.

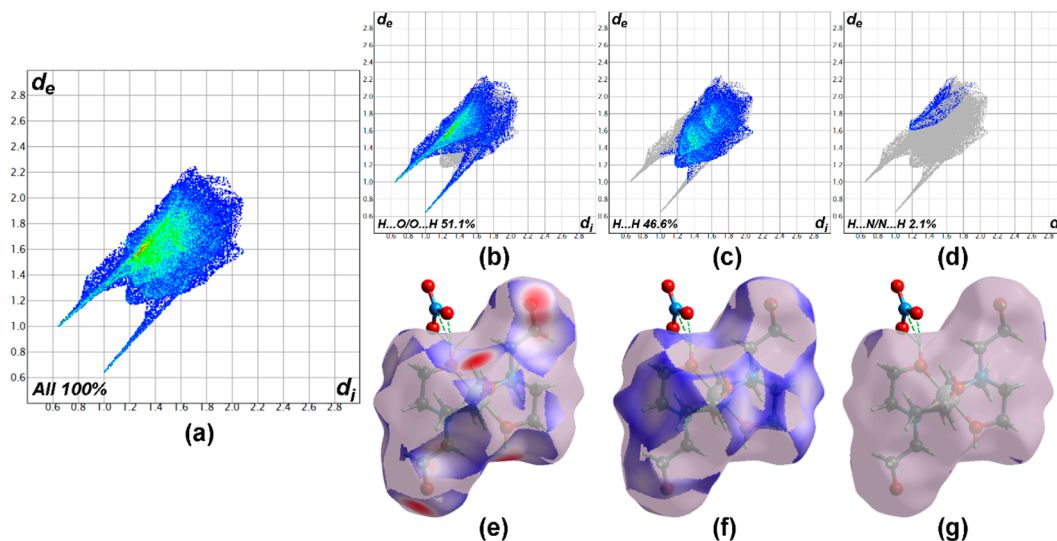


Figure 3. The full two-dimensional fingerprint plot for the Ni-TEA compound, showing (a) all interactions and those delineated into (b) $H\cdots O/O\cdots H$, (c) $H\cdots H$ and (d) $H\cdots N/N\cdots H$ interactions. The d_i and d_e values are the closest internal and external distances (in \AA) from given points on the Hirshfeld surface (HS). The corresponding HS for (e) $H\cdots O/O\cdots H$, (f) $H\cdots H$, and (g) $H\cdots N/N\cdots H$ is plotted over the d_{norm} range from -0.7343 to 1.2167 a.u.

3.4. Characteristic Features of the Ni-TEA Complex

Fourier transform infrared (FTIR) spectrum of the Ni-TEA complex is illustrated in Figure 4. Several peaks regarding O–H stretching were observed at a wavenumber higher than 3100 cm^{-1} (i.e., at 3118 , 3176 , 3355 and 3408 cm^{-1}), due to the presence of OH groups with different chemical environments. The peak at 3118 cm^{-1} is assigned to the weakly-bound hydroxyl groups, which might be assigned to $O3\cdots O5$ and $O3\cdots O6$ interactions with interatomic distances from $2.9533(15)$ to $2.9535(16) \text{ \AA}$ (Table 2). The estimation of its wavenumber by the empirical relationship between $O\cdots O$ distances and stretching OH frequencies by Bellamy and Owen [67] gives the value of 3140 cm^{-1} , which is well matched with the observed wavenumber in this study. The other two peaks at 3355 and 3408 cm^{-1} are attributed to the strongly bound OH groups with shorter $O\cdots O$ interatomic distances (i.e., $O1\cdots O4$ and $O2\cdots O3$, respectively) (Table 2). Apart from the OH vibrations, the characteristic peaks of sp^3 -hybridized CH_2 groups were observed at the wavenumber slightly below 3000 cm^{-1} (2969 , 2923 and 2899 cm^{-1}). The strongest peak in the spectrum was found at 1384 cm^{-1} , which corresponded to the nitrate counter ions. Note that this FTIR band was also observed in the $[\text{Co}(\text{TEA})_2](\text{NO}_3)_2$ complex (at 1380 cm^{-1}) and reported by others [68]. Therefore, the FTIR results confirm the formation of the hydrogen bonding framework in the crystal of the Ni-TEA complex, which agrees with the obtained data from the SC-XRD.

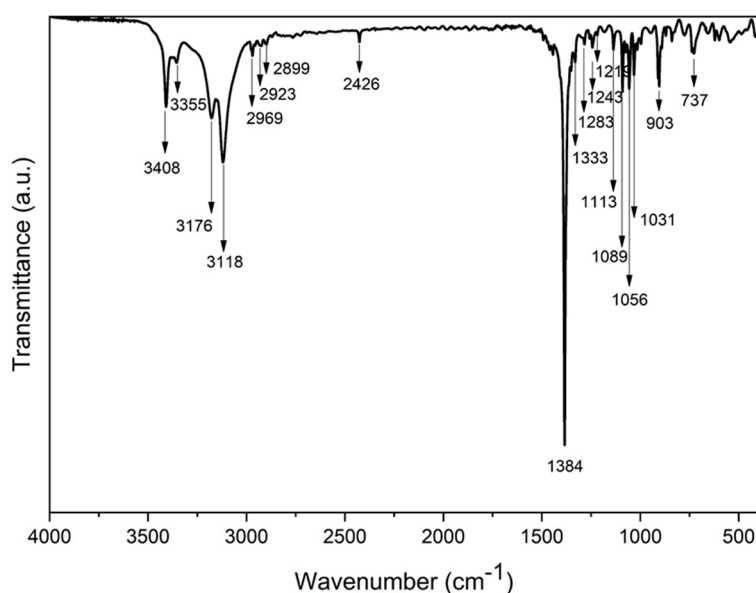


Figure 4. Fourier transformed infrared spectroscopy (FTIR) spectrum of the Ni-TEA complex.

In order to clarify the crystallite homogeneity of the obtained Ni-TEA products, synchrotron powder X-ray diffraction (XRD) was carried out using the monochromatic X-ray with a photon energy of 12 keV. The comparison of XRD patterns (Figure 5) indicates a good agreement of the peak positions and intensities between the Ni-TEA crystals prepared by the standard procedure reported herein and by employing electrochemical study. This result emphasizes the consistency of the complex preparation. Note that a slight deviation of the XRD patterns of the crystals from the calculated pattern generated by the SC-XRD data is negligible, which indicates a high degree of crystallinity of the obtained Ni-TEA crystals.

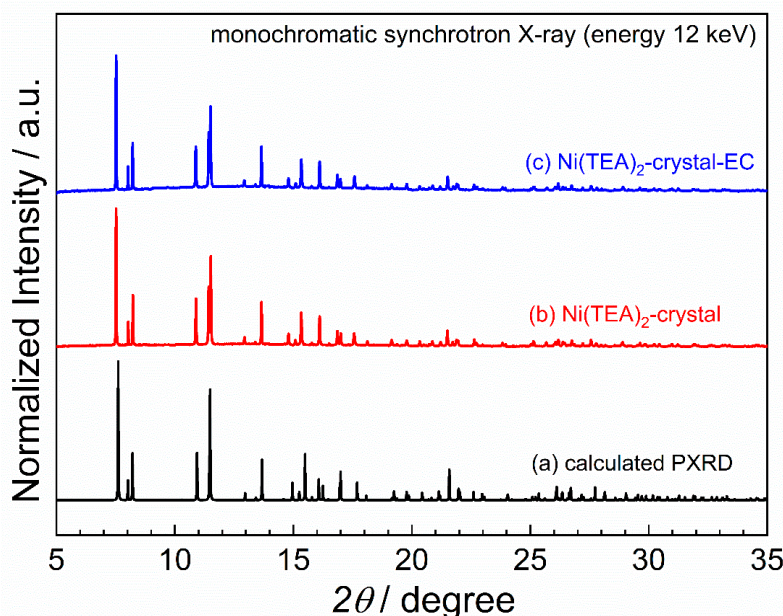


Figure 5. Powder XRD diffraction patterns comparing (a) the calculated pattern from SC-XRD data, (b) the crystal of bis(triethanolamine)nickel(II) dinitrate complex and (c) the corresponding crystal obtained from electrochemical studies.

Moreover, the elemental compositions were analyzed by employing WD-XRF technique in order to clarify the purity of the product. The weight ratio of C, N, O and Ni elements of the bulk Ni-TEA

product was well-matched to the calculated data (excluding H atoms) derived from the chemical formula of the Ni-TEA single crystal (Table 3). This result clearly indicates the high purity of the obtained Ni-TEA crystal with less contribution of the non-crystalline impurities. Consequently, it highlights the successful preparation of the targeted Ni-TEA crystal.

Table 3. Elemental compositions of the obtained Ni-TEA crystals examined by wavelength dispersive X-ray fluorescence (WD-XRF) compared to the calculated data derived from the Ni-TEA single crystal (excluding H atoms).

Elements	Elemental Composition (Excluding H atoms) (% Weight)				
	Calculated Data from Single Crystal	XRF Data of the Obtained Ni-TEA Crystals			
		1st	2nd	3rd	Averaged
C	31.97	29.63	31.13	31.40	30.72 ± 0.78
N	12.43	12.78	12.75	13.25	12.93 ± 0.23
O	42.58	44.34	42.73	41.26	42.77 ± 1.26
Ni	13.02	13.25	13.39	14.09	13.58 ± 0.37

3.5. Quantum Chemical Calculations

The DFT calculations of the Ni-TEA complex were carried out by employing the PBE0/6-311G(d,p) level of theory in the ethanolic solvent system. The optimized geometrical parameters, such as bond lengths (Å) and bond angles (°) are listed in Table 4. It was observed that the DFT-optimized structural parameters represent a good approximation of the experimental data and can be further used as a foundation to calculate the other spectroscopic information for the Ni-TEA compound.

Table 4. Structural parameters of the Ni-TEA complex, which is experimentally derived from the SC-XRD data and theoretically obtained by the DFT calculation.

Parameters	X-ray Crystallography	DFT Calculations
Bond Lengths (Å)		
Ni1-O1	2.0519(8)	1.868
Ni1-O1 ¹	2.0519(9)	1.864
Ni1-O2	2.0751(9)	1.872
Ni1-O2 ¹	2.0751(9)	1.867
Ni1-N1	2.1021(10)	1.979
Ni1-N1 ¹	2.1021(10)	1.971
Bond Angles (°)		
O1-Ni1-O2	93.07(4)	88.12
O1-Ni1-O1 ¹	180.0	175.68
O1 ¹ -Ni1-O2	86.92(4)	92.36
C4-O2-Ni1	106.51(6)	110.94
C3-N1-Ni1	107.50(6)	102.38
N1-Ni1-N1 ¹	180.0	177.61

¹ The atoms generated by inversion symmetry.

To further investigate the electronic structures and excitations of the complex, theoretical calculations were performed in an ethanolic solvent using a PBE0/6-311G(d,p) basis set and the PCM approach was applied. Moreover, the time-dependent density functional theory (TD-DFT) was used for predicting the absorption spectra of the Ni-TEA complex. As a result, ten excited states and the wavelengths of the electronic absorption spectra of the Ni-TEA complex are reported in Table 5.

Table 5. The lowest excitation energies in eV and oscillator strength (f) in the solvent phase (in ethanol) using the TD-PBE0/6-311G(d,p) method for the Ni-TEA complex. The highest occupied molecular orbital (HOMO) is donated by H and L is the lowest unoccupied molecular orbital (LUMO).

States	eV	nm	f	Transition State
$S_0 \rightarrow S_5$	2.38	521	0.0015	HOMO \rightarrow LUMO (72%) + HOMO \rightarrow L+1 (18%)
$S_0 \rightarrow S_6$	2.45	506	0.0028	H-1 \rightarrow LUMO (66%) + H-1 \rightarrow L+1 (23%)
$S_0 \rightarrow S_9$	3.08	402	0.0358	HOMO \rightarrow L+1 (33%) + HOMO \rightarrow LUMO (22%)
$S_0 \rightarrow S_{10}$	3.19	388	0.0435	H-1 \rightarrow LUMO (23%) + H-1 \rightarrow L+1 (22%)

The strong electronic absorptions were observed at $\lambda_{\max} = 388$ nm (with the oscillator strengths (f) of 0.0435) and at $\lambda_{\max} = 402$ nm (with $f = 0.0358$), which can be assigned to the electronic transitions of $S_0 \rightarrow S_{10}$ and $S_0 \rightarrow S_9$, respectively. The $S_0 \rightarrow S_{10}$ transition consists of two main configurations, namely H-1 \rightarrow LUMO and H-1 \rightarrow L+1, while the $S_0 \rightarrow S_9$ transition possesses HOMO \rightarrow LUMO and HOMO \rightarrow L+1 configuration. Note that the calculated data corresponded to the experimental absorption spectrum of the ethanolic solution of the Ni-TEA complex (1×10^{-5} mol L $^{-1}$) as shown in Figure 6. Specifically, the experimental UV absorption peak was found at $\lambda_{\max} = 404$ nm, while the quantum calculation showed the two peaks at $\lambda_{\max} = 388$ and 402 nm.

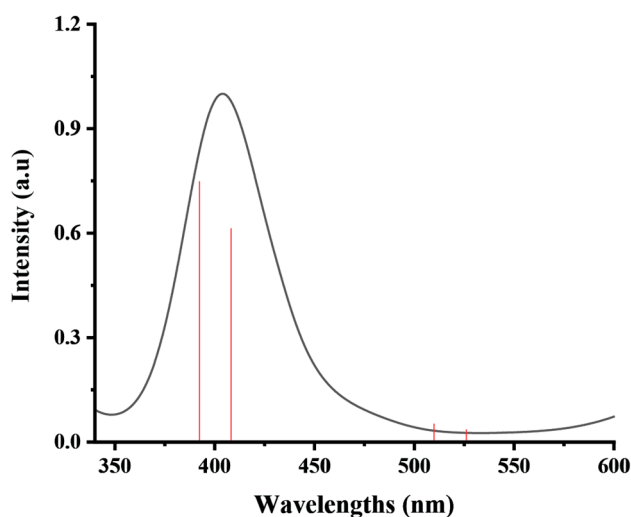


Figure 6. Experimental UV-VIS absorption spectrum of the Ni-TEA complex (black) measured in the form of ethanolic solution (1×10^{-5} mol L $^{-1}$) and its corresponding DFT calculated data (red).

Molecular orbitals (MOs), which represent the total wavefunction of the system, can provide valuable insight into bonding interactions. Hence, the frontier molecular orbitals (FMOs) were analyzed in order to understand the electronic transitions. Visualization of the FMOs of the Ni-TEA complex so-called the HOMO, LUMO, H-1 and L+1 are illustrated in Figure 7. Interestingly, the FMOs of the Ni-TEA complex were mainly located on the TEA ligands. Therefore, it can be concluded that the electronic transitions of the complex originated from the transition within the ligand.

3.6. Thermal Analysis

The thermogravimetric (TGA) and differential thermal analyses (DTA) were carried out in the temperature range from 50 to 400 °C to observe the thermal event that occurred upon heating (Figure 8). According to the TGA thermogram, the first thermal decomposition was observed at a temperature of 242 °C, which could possibly be triggered by the decomposition of the nitrate groups. Further decomposition was assigned to the oxidation of the carbonaceous compositions to form CO and CO $_2$ gases. This information supports the structural composition of the Ni-TEA complex derived by SC-XRD. The thermal decomposition apparently finished at a temperature of 380 °C, providing a

residue weight of 16.28% with respect to the starting mass of the complex. This observation clearly indicates the formation of nickel oxides, mainly NiO, of which the theoretical ceramic yield was 15.52% after thermal decomposition of the Ni-TEA complex as shown in the equation below:

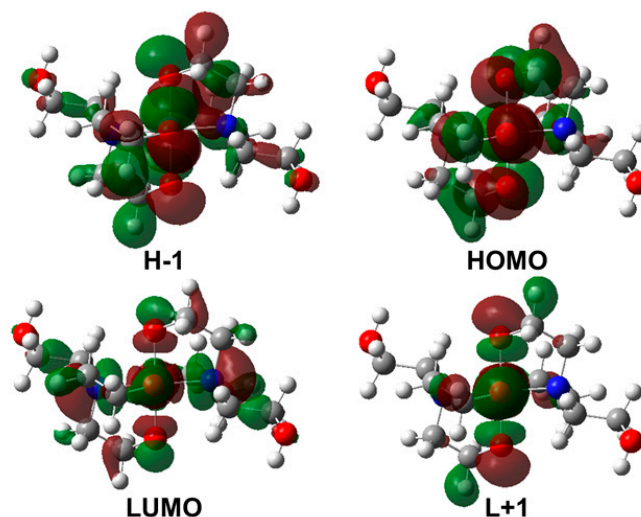


Figure 7. Visualization of the frontier molecular orbitals (FMOs) of the Ni-TEA complex calculated using the TD-PBE0/6-311G(d,p) method.

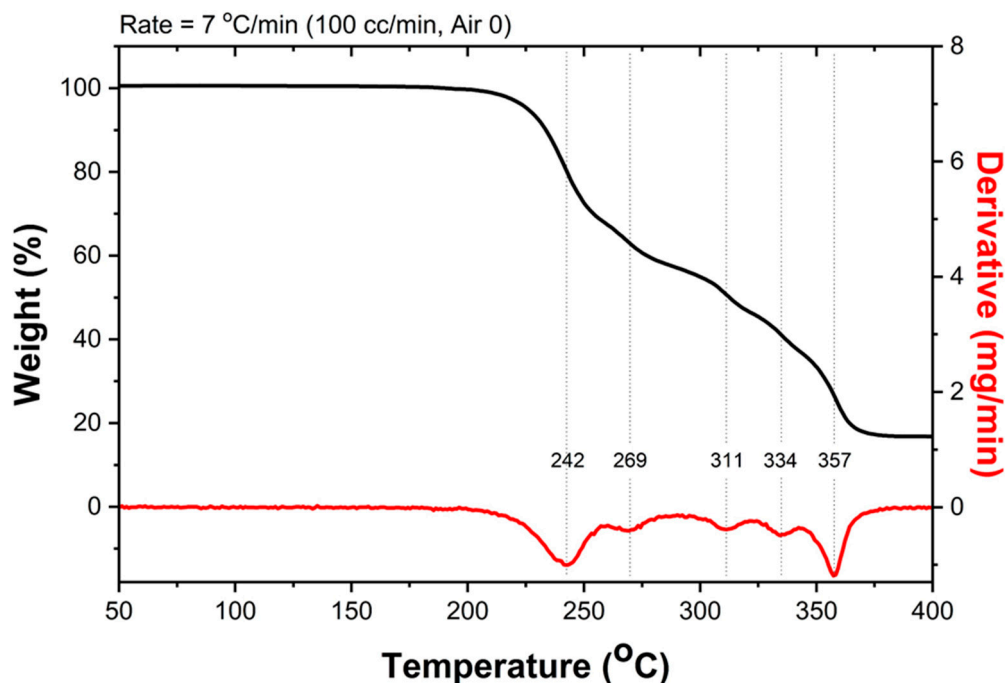


Figure 8. Thermal gravimetric analysis (TGA) and DTA thermograms of the Ni-TEA complex.

3.7. Electrochemical Study

Cyclic voltammetry (CV) during the mixing of the ethanolic solutions of $\text{Ni}(\text{NO}_3)_2 \cdot 6\text{H}_2\text{O}$ and TEA ligand to form the Ni-TEA complex was measured in the potential window from -1.0 to $+1.0$ V and then compared to the CV of the ethanolic solutions of pristine $\text{Ni}(\text{NO}_3)_2 \cdot 6\text{H}_2\text{O}$. Interestingly, the

anodic peak was observed in the cyclic voltammogram of the Ni-TEA complex mixture (Figure 9a (1)), whereas no oxidation peak of the $\text{Ni}(\text{NO}_3)_2 \cdot 6\text{H}_2\text{O}$ was observed in the measured potential range (Figure 9a (2)). The oxidation peak observed in the case of the complex mixture corresponded to the irreversible oxidation process of Ni^{2+} to Ni^{3+} at $E_{\text{pa}} = 0.72$ V, which has been observed in other Ni-complex systems reported in the literature [69,70]. Moreover, voltammogram of the TEA ligand was investigated in ethanol and gave an oxidation peak potential at 1.530 V without the presence of a cathodic wave, as shown in Figure 9b. This observation emphasizes that the Ni-TEA complex exhibits oxidation at a lower potential than both the metal ions and the TEA precursor solutions. Moreover, the oxidation peak at $E_{\text{pa}} = 0.72$ V presented in the CV of the Ni-TEA complex is not exactly the oxidation peak of the TEA ligand itself but rather the oxidation of the complex. It should be noted that the oxidation process of $\text{Ni}^{2+}/\text{Ni}^{3+}$ that occurred in the nickel complexes relies on the coordinated ligands [71]. Moreover, the electrochemical oxidation of the Ni^{2+} into Ni^{3+} -complex by applying constant overpotential was previously reported in another Ni^{2+} complex system [72].

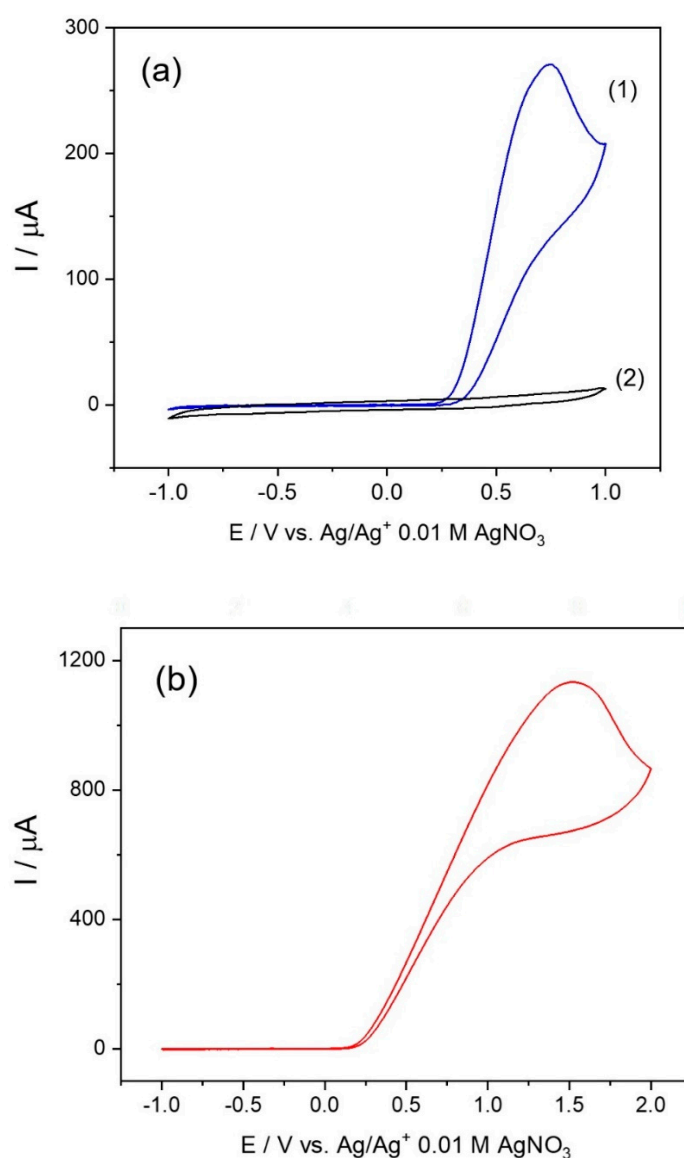


Figure 9. Cyclic voltammograms at the scan rate of 100 mV/s for (a) (1) the formation of the $[\text{Ni}(\text{TEA})_2]^{2+}$ complex by adding 0.2 M $\text{Ni}(\text{NO}_3)_2 \cdot 6\text{H}_2\text{O}$ into 0.4 M TEA (1:1 by volume) compared to (2) 0.2 M $\text{Ni}(\text{NO}_3)_2 \cdot 6\text{H}_2\text{O}$ and (b) 0.2 M TEA in ethanol. Note that 0.1 M LiClO_4 in ethanol was used as the electrolyte.

As the oxidation potential of the Ni-TEA complex was significantly lower than the one of nickel(II) nitrate hexahydrate, it would be feasible to use the Ni-TEA complex to prepare metal and/or mixed metal oxides composed of mixed +2 and +3 oxidation states of Ni species. Additionally, the Ni-TEA complex might be applied as one of the promising precursors for the preparation of mixed metal spinel and perovskite materials, in which the oxidation state and the site occupancy of the targeted metal ions can be tailored and controlled.

4. Conclusions

This work reported the successful synthesis of bis(triethanolamine)nickel(II) dinitrate complex (so-called Ni-TEA complex) thorough investigation of its crystal structure and characteristic features. Based on the SC-XRD data of the complex, the distorted octahedral inner sphere coordination of the Ni central ion is formed by two neutral ($\kappa^3\text{-N,O,O'}$)tridentate TEA ligands. The two nitrate ions that act as charge compensation are located at the outer-sphere coordination. A variety of O-H...O hydrogen bonding interactions between the motifs are found to be the major contributors to the crystal packing, which is clearly indicated by the fingerprint plot of the Hirshfeld surface analysis and the various O-H stretching FTIR bands. The DFT calculations using the PBE0/6-311G(d,p) level of theory reveal that the electronic transitions of the Ni-TEA complex in an ethanolic solvent originated from transition within the ligand. The residue mass and thermogravimetric profile suggest that the Ni-TEA complex could be a promising precursor for the synthesis of metal oxide materials via thermal decomposition. Interestingly, the oxidation potential based on the cyclic voltammogram of the Ni-TEA complex provides feasibility to tailor and control the oxidation state and the site occupancy of the targeted Ni components within the mixed metal materials such as the ones possessing spinel and perovskite structures. Consequently, the targeted material properties could be rationally designed.

Author Contributions: S.W., P.P. (Pinyou) and W.W. planned the experiment; W.D., S.W., Y.H., P.P. (Pinyou) and W.W. wrote the original draft of the manuscript; W.D., P.P. (Pansiri) and P.K. prepared the sample; W.D., S.W., P.P. (Pansiri), P.K., Y.H., P.P. (Pinyou) and W.W. performed the characterization measurements; A.L. and K.P. provided certain facilities and equipment; S.S. carried out a computational study; S.W., P.P. (Pinyou) and W.W. did the data analysis. All authors have read and agreed to the published version of the manuscript.

Funding: This research received no external funding.

Acknowledgments: The Department of Materials Engineering, Faculty of Engineering, Kasetsart University, and the School of Chemistry, Institute of Science, Suranaree University of Technology are acknowledged for the support of the facilities. We acknowledge the Synchrotron Light Research Institute (Public Organization), SLRI, Thailand, for the provision of beamtime for XRD at BL1.1W. All research staffs of BL1.1W are acknowledged for their assistance during the experiment.

Conflicts of Interest: The authors declare no conflict of interest.

References

1. Seisenbaeva, G.A.; Kessler, V.G. Precursor directed synthesis—"molecular" mechanisms in the Soft Chemistry approaches and their use for template-free synthesis of metal, metal oxide and metal chalcogenide nanoparticles and nanostructures. *Nanoscale* **2014**, *6*, 6229–6244. [[CrossRef](#)] [[PubMed](#)]
2. Abdel-Fatah, S.M.; Sánchez, M.D.; Díaz-García, D.; Prashar, S.; Abdel-Rahman, L.H.; Gómez-Ruiz, S. Nanostructured metal oxides prepared from schiff base metal complexes: Study of the catalytic activity in selective oxidation and C–C coupling reactions. *J. Inorg. Organomet. Polym. Mater.* **2019**, *30*, 1293–1305. [[CrossRef](#)]
3. Lu, H.; Wright, D.S.; Pike, S.D. The use of mixed-metal single source precursors for the synthesis of complex metal oxides. *Chem. Commun.* **2020**, *56*, 854–871. [[CrossRef](#)]
4. Polarz, S.; Orlov, A.V.; Berg, M.W.E.V.D.; Driess, M. Molecular encoding at the nanoscale: From complex cubes to bimetallic oxides. *Angew. Chem. Int. Ed.* **2005**, *44*, 7892–7896. [[CrossRef](#)] [[PubMed](#)]

5. Pfrommer, J.; Lublow, M.; Azarpira, A.; Göbel, C.; Lücke, M.; Steigert, A.; Pogrzeba, M.; Menezes, P.W.; Fischer, A.; Schedel-Niedrig, T.; et al. A molecular approach to self-supported cobalt-substituted ZnO materials as remarkably stable electrocatalysts for water oxidation. *Angew. Chem. Int. Ed.* **2014**, *53*, 5183–5187. [[CrossRef](#)]
6. Pfrommer, J.; Azarpira, A.; Steigert, A.; Olech, K.; Menezes, P.W.; Duarte, R.F.; Liao, X.; Wilks, R.G.; Bär, M.; Schedel-Niedrig, T.; et al. Active and stable nickel-based electrocatalysts based on the ZnO:Ni system for water oxidation in alkaline media. *ChemCatChem* **2016**, *9*, 672–676. [[CrossRef](#)]
7. Rao, C.N.R. Chemical approaches to the design of oxide materials. *Pure Appl. Chem.* **1994**, *66*, 1765–1772. [[CrossRef](#)]
8. Huang, X.; Zhao, G.; Wang, G.; Irvine, J.T.S. Synthesis and applications of nanoporous perovskite metal oxides. *Chem. Sci.* **2018**, *9*, 3623–3637. [[CrossRef](#)]
9. Naiini, A.A.; Pinkas, J.; Plass, W.; Young, V.G.; Verkade, J.G. Triethanolamine Complexes of H⁺, Li⁺, Na⁺, Sr²⁺, and Ba²⁺ Perchlorates. *Inorg. Chem.* **1994**, *33*, 2137–2141. [[CrossRef](#)]
10. Naiini, A.A.; Young, V.G.; Verkade, J.G. Alkali and alkaline earth metal chloride complexes of triethanolamine: The structure of [Sr(TEA)₂]Cl₂. *Polyhedron* **1997**, *16*, 2087–2092. [[CrossRef](#)]
11. Yilmaz, V.T.; Senel, E.; Thöne, C. Synthesis, spectral, thermal and structural characterization of {[Cu(H₂O)₃][Cu(MAL)₂·2H₂O]_∞ and [Cu(MAL)(TEA)]·H₂O (MAL = malonate and TEA = triethanolamine). *Transit. Met. Chem.* **2004**, *29*, 336–342. [[CrossRef](#)]
12. Ashurov, J.; Ibragimov, A.; Ibragimov, B. Mixed-ligand complexes of Zn(II), Cd(II) and Cu(II) with triethanolamine and p-nitrobenzoic acid: Syntheses and crystal structures. *Polyhedron* **2015**, *102*, 441–446. [[CrossRef](#)]
13. Wattanathana, W.; Nootsuwan, N.; Veranitisagul, C.; Koonsaeng, N.; Laosiripojana, N.; Laobuthee, A. Simple cerium-triethanolamine complex: Synthesis, characterization, thermal decomposition and its application to prepare ceria support for platinum catalysts used in methane steam reforming. *J. Mol. Struct.* **2015**, *1089*, 9–15. [[CrossRef](#)]
14. Naiini, A.A.; Young, V.; Verkade, J.G. New complexes of triethanolamine (Tea): Novel structural features of [Y(TEA)₂](ClO₄)₃·3C₅H₅N and [Cd(TEA)₂](NO₃)₂. *Polyhedron* **1995**, *14*, 393–400. [[CrossRef](#)]
15. Ashurov, J.M. Crystal structure of the salt bis-(tri-ethano-lamine-κ(4) N,O,O',O'')cadmium bis[2-(2-oxo-2,3-di-hydro-1,3-benzo-thia-zol-3-yl)acetate]. *Acta Crystallogr. Sect. E Crystallogr. Commun.* **2016**, *72*, 526–529. [[CrossRef](#)] [[PubMed](#)]
16. Krabbes, I.; Seichter, W.; Gloe, K. Bis(triethanolamine-O,O')nickel(II) diacetate. *Acta Crystallogr. Sect. C Cryst. Struct. Commun.* **2000**, *56*. [[CrossRef](#)]
17. Topcu, Y.; Andaç, Ö.; Yilmaz, V.T.; Harrison, W.T.A. Bis(triethanolamine-N,O,O')nickel(II) bis(saccharinate). *Acta Crystallogr. Sect. E Struct. Rep. Online* **2001**, *57*, m82–m84. [[CrossRef](#)]
18. Topcu, Y.; Andaç, Ö.; Yilmaz, V.T.; Harrison, W.; Yilmaz, V. Synthesis, characterization and spectral studies of triethanolamine complexes of metal saccharinates. Crystal structures of [Co(TEA)₂](SAC)₂ AND [Cu₂(μ-TEA)₂](SAC)₂·2(CH₃OH). *J. Coord. Chem.* **2002**, *55*, 805–815. [[CrossRef](#)]
19. Uçar, I.; Yeşilel, O.Z.; Bulut, A.; Icbudak, H.; Ölmez, H.; Kazak, C. Bis(triethanolamine-κ 3N,O,O')copper(II) squarate. *Acta Crystallogr. Sect. E Struct. Rep. Online* **2004**, *60*. [[CrossRef](#)]
20. Haukka, M.; Kirillov, A.M.; Kopylovich, M.N.; Pombeiro, A.J.L. Bis(triethanolamine-κ 3N, O, O')nickel(II) benzene-1,4-dicarboxylate. *Acta Crystallogr. Sect. E Struct. Rep. Online* **2005**, *61*. [[CrossRef](#)]
21. Yeşilel, O.Z.; Ölmez, H.; Uçar, I.; Bulut, A.; Kazak, C. Synthesis, spectrothermal behaviour and molecular structure of Aquaorotatotriethanolaminenickel(II) monohydrate. *Zeitschrift für anorganische und allgemeine Chemie* **2005**, *631*, 3100–3103. [[CrossRef](#)]
22. Ashurov, J.M.; Obidova, N.J.; Abdireymov, H.B.; Ibragimov, B. Crystal structure of the salt bis-(tri-ethano-lamine-κ(3) N,O,O')cobalt(II) bis-[2-(2-oxo-2,3-di-hydro-1,3-benzo-thia-zol-3-yl)acetate]. *Acta Crystallogr. Sect. E Crystallogr. Commun.* **2016**, *72*, 420–423. [[CrossRef](#)]
23. Andaç, Ö.; Topcu, Y.; Yilmaz, V.T.; Guven, K. Bis(triethanolamine)cadmium(II) and -mercury(II) saccharinates: Seven-coordinate complexes containing both tri- and tetradentate triethanolamine ligands. *Acta Crystallogr. Sect. C Cryst. Struct. Commun.* **2001**, *57*, 1381–1384. [[CrossRef](#)] [[PubMed](#)]
24. Atria, A.M.; Parada, J.; Garland, M.T.; Baggio, R. A Cu(II) polymeric complex surveying triethanolamine and 1,2-di(4-pyridyl)ethylene as bridging ligands. *J. Chil. Chem. Soc.* **2015**, *60*, 3059–3062. [[CrossRef](#)]

25. Kirillov, A.M.; Kopylovich, M.N.; Kirillova, M.V.; Haukka, M.; Da Silva, M.F.C.G.; Pombeiro, A.J.L. Multinuclear copper triethanolamine complexes as selective catalysts for the peroxidative oxidation of alkanes under mild conditions. *Angew. Chem. Int. Ed.* **2005**, *44*, 4345–4349. [[CrossRef](#)] [[PubMed](#)]
26. Zhu, M.; Wei, X.; Li, B.; Yuan, Y. Copper-triethanolamine complex as efficient and active catalyst for selective oxidation of alkylarenes to phenyl ketones by tert-butylhydroperoxide. *Tetrahedron Lett.* **2007**, *48*, 9108–9111. [[CrossRef](#)]
27. Sampaio, R.N.; Grills, D.C.; Polyansky, D.E.; Szalda, D.J.; Fujita, E. Unexpected roles of triethanolamine in the photochemical reduction of CO₂ to formate by ruthenium complexes. *J. Am. Chem. Soc.* **2019**, *142*, 2413–2428. [[CrossRef](#)] [[PubMed](#)]
28. Morimoto, T.; Nakajima, T.; Sawa, S.; Nakanishi, R.; Imori, D.; Ishitani, O. CO₂ capture by a Rhenium(I) complex with the aid of triethanolamine. *J. Am. Chem. Soc.* **2013**, *135*, 16825–16828. [[CrossRef](#)]
29. Koizumi, H.; Chiba, H.; Sugihara, A.; Iwamura, M.; Nozaki, K.; Ishitani, O. CO₂ capture by Mn(i) and Re(i) complexes with a deprotonated triethanolamine ligand. *Chem. Sci.* **2019**, *10*, 3080–3088. [[CrossRef](#)]
30. Boursourani, Z.; Geromichalos, G.; Repana, K.; Yiannaki, E.; Psycharis, V.; Raptopoulou, C.P.; Hadjipavlou-Litina, D.; Pontiki, E.; Dendrinou-Samara, C. Preparation and pharmacochemical evaluation of mixed ligand copper(II) complexes with triethanolamine and thiophenyl-2 saturated carboxylic acids. *J. Inorg. Biochem.* **2011**, *105*, 839–849. [[CrossRef](#)]
31. Park, Y.; Kim, C.; Lee, H. Effects of catalyst and solvent on PbTiO₃ fibers prepared from triethanolamine complexed titanium isopropoxide. *J. Sol-Gel Sci. Technol.* **1999**, *14*, 149–162. [[CrossRef](#)]
32. Laobuthee, A.; Wongkasemjit, S.; Traversa, E.; Laine, R.M. MgAl₂O₄ spinel powders from oxide one pot synthesis (OOPS) process for ceramic humidity sensors. *J. Eur. Ceram. Soc.* **2000**, *20*, 91–97. [[CrossRef](#)]
33. Wattanathana, W.; Lakkham, A.; Kaewvilai, A.; Koonsaeng, N.; Laobuthee, A.; Veranitisagul, C. Preliminary study of Pd/CeO₂ derived from cerium complexes as solid support catalysts for hydrogenation reaction in a micro-reactor. *Energy Procedia* **2011**, *9*, 568–574. [[CrossRef](#)]
34. Wattanathana, W.; Wannapaiboon, S.; Veranitisagul, C.; Laosiripojana, N.; Koonsaeng, N.; Laobuthee, A. Preparation of palladium-impregnated ceria by metal complex decomposition for methane steam reforming catalysis. *Adv. Mater. Sci. Eng.* **2017**, *2017*, 1–10. [[CrossRef](#)]
35. Wattanathana, W.; Veranitisagul, C.; Wannapaiboon, S.; Klysubun, W.; Koonsaeng, N.; Laobuthee, A. Samarium doped ceria (SDC) synthesized by a metal triethanolamine complex decomposition method: Characterization and an ionic conductivity study. *Ceram. Int.* **2017**, *43*, 9823–9830. [[CrossRef](#)]
36. Nantharak, W.; Wattanathana, W.; Klysubun, W.; Rimpongpisarn, T.; Veranitisagul, C.; Koonsaeng, N.; Laobuthee, A. Effect of local structure of Sm³⁺ in MgAl₂O₄:Sm³⁺ phosphors prepared by thermal decomposition of triethanolamine complexes on their luminescence property. *J. Alloy. Compd.* **2017**, *701*, 1019–1026. [[CrossRef](#)]
37. Haron, W.; Thaweechai, T.; Wattanathana, W.; Laobuthee, A.; Manaspiya, H.; Veranitisagul, C.; Koonsaeng, N. Structural characteristics and dielectric properties of La_{1-x}CoxFeO₃ and LaFe_{1-x}CoxO₃ synthesized via metal organic complexes. *Energy Procedia* **2013**, *34*, 791–800. [[CrossRef](#)]
38. Rimpongpisarn, T.; Wattanathana, W.; Sukthavorn, K.; Nootsuwan, N.; Hanlumyung, Y.; Veranitisagul, C.; Laobuthee, A. Novel luminescent PLA/MgAl₂O₄:Sm³⁺ composite filaments for 3D printing application. *Mater. Lett.* **2019**, *237*, 270–273. [[CrossRef](#)]
39. Laobuthee, A.; Veranitisagul, C.; Wattanathana, W.; Koonsaeng, N.; Laosiripojana, N. Activity of Fe supported by Ce_{1-x}Sm_xO_{2-δ} derived from metal complex decomposition toward the steam reforming of toluene as biomass tar model compound. *Renew. Energy* **2015**, *74*, 133–138. [[CrossRef](#)]
40. Veranitisagul, C.; Wattanathana, W.; Nantharak, W.; Jantaratana, P.; Laobuthee, A.; Koonsaeng, N. BaFe₁₂O₁₉ from thermal decomposition of bimetallic triethanolamine complex as magnetic filler for bioplastics. *Mater. Chem. Phys.* **2016**, *177*, 48–55. [[CrossRef](#)]
41. Hieber, W.; Levy, E. Das komplexchemische Verhalten der Äthylolamine. II. *Zeitschrift für anorganische und allgemeine Chemie* **1934**, *219*, 225–237. [[CrossRef](#)]
42. Nielsen, K.; Hazell, R.G.; Rasmussen, S.E.; Larsson, R.; Norden, B.; Sundbom, M. The crystal structure of Di-triethanolamine-Ni(II)-dinitrate. *Acta Chem. Scand.* **1972**, *26*, 889–896. [[CrossRef](#)]
43. SAINT. *Version 8.34A 2013*; Bruker AXS: Madison, WI, USA, 2013.
44. Sheldrick, G.M. *SADABS*; University of Göttingen: Göttingen, Germany, 1996.

45. Dolomanov, O.; Bourhis, L.J.; Gildea, R.; Howard, J.A.; Puschmann, H. OLEX2: A complete structure solution, refinement and analysis program. *J. Appl. Crystallogr.* **2009**, *42*, 339–341. [[CrossRef](#)]
46. Sheldrick, G.M. SHELXT—Integrated space-group and crystal-structure determination. *Acta Crystallogr. Sect. A Found. Adv.* **2015**, *71*, 3–8. [[CrossRef](#)] [[PubMed](#)]
47. Sheldrick, G.M. Crystal structure refinement with SHELXL. *Acta Crystallogr. Sect. C Struct. Chem.* **2015**, *71*, 3–8. [[CrossRef](#)] [[PubMed](#)]
48. Macrae, C.; Edgington, P.R.; McCabe, P.E.; Pidcock, E.; Shields, G.; Taylor, R.; Towler, M.; Van De Streek, J. Mercury: Visualization and analysis of crystal structures. *J. Appl. Crystallogr.* **2006**, *39*, 453–457. [[CrossRef](#)]
49. Barboza, C.A.; Germino, J.C.; Santana, A.M.; Quites, F.J.; Vazquez, P.A.M.; Atvars, T.D.Z. Structural correlations between luminescent properties and excited state internal proton transfer in some Zinc(II)*N,N'*-Bis(salicylidenes). *J. Phys. Chem. C* **2015**, *119*, 6152–6163. [[CrossRef](#)]
50. Vivas, M.; Germino, J.C.; Barboza, C.A.; Vazquez, P.; De Boni, L.; Atvars, T.D.Z.; Mendonça, C.R. Excited-state and two-photon absorption in salicylidene molecules: The role of Zn(II) planarization. *J. Phys. Chem. C* **2016**, *120*, 4032–4039. [[CrossRef](#)]
51. Perdew, J.P.; Burke, K.; Ernzerhof, M. Generalized gradient approximation made simple. *Phys. Rev. Lett.* **1996**, *77*, 3865–3868. [[CrossRef](#)]
52. Raghavachari, K.; Trucks, G.W. Highly correlated systems. Excitation energies of first row transition metals Sc–Cu. *J. Chem. Phys.* **1989**, *91*, 1062–1065. [[CrossRef](#)]
53. Krishnan, R.; Binkley, J.S.; Seeger, R.; Pople, J.A. Self-consistent molecular orbital methods. XX. A basis set for correlated wave functions. *J. Chem. Phys.* **1980**, *72*, 650. [[CrossRef](#)]
54. Frisch, M.J.; Trucks, G.W.; Schlegel, H.B.; Scuseria, G.E.; Robb, M.A.; Cheeseman, J.R.; Scalmani, G.; Barone, V.; Mennucci, B.; Petersson, G.A.; et al. *Gaussian 09, Revision B. 01*; Gaussian Inc: Wallingford, CT, USA, 2010.
55. Scalmani, G.; Frisch, M.J.; Mennucci, B.; Tomasi, J.; Cammi, R.; Barone, V. Geometries and properties of excited states in the gas phase and in solution: Theory and application of a time-dependent density functional theory polarizable continuum model. *J. Chem. Phys.* **2006**, *124*, 094107. [[CrossRef](#)] [[PubMed](#)]
56. Mennucci, B.; Cappelli, C.; Guido, C.A.; Cammi, R.; Tomasi, J. Structures and properties of electronically excited chromophores in solution from the polarizable continuum model coupled to the time-dependent density functional theory. *J. Phys. Chem. A* **2009**, *113*, 3009–3020. [[CrossRef](#)] [[PubMed](#)]
57. Içbudak, H.; Yılmaz, V.T.; Howie, R.A.; Andaç, Ö.; Ölmez, H. Bis[tris(2-hydroxyethyl)amine]nickel(II) Chloride. *Acta Crystallogr. Sect. C Cryst. Struct. Commun.* **1995**, *51*, 1759–1761. [[CrossRef](#)]
58. Yeşilel, O.Z.; Bulut, A.; Uçar, I.; Içbudak, H.; Ölmez, H.; Büyükgüngör, O. Bis(triethanolamine- κ^3N,O,O') nickel(II) squarate. *Acta Crystallogr. Sect. E Struct. Rep. Online* **2004**, *60*, m228–m230. [[CrossRef](#)]
59. Fundamensky, V.; Kochina, T.; Kondratenko, Y.; Zolotarev, A.A.; Vlasov, Y.; Ignatyev, I. Ionic liquids based on triethanolammonium salts of dicarboxylic acids (oxalic, malonic, succinic). Crystal structure and cation-anion interaction. *J. Mol. Liq.* **2017**, *230*, 113–120. [[CrossRef](#)]
60. Etter, M.C.; Macdonald, J.C.; Bernstein, J. Graph-set analysis of hydrogen-bond patterns in organic crystals. *Acta Crystallogr. Sect. B Struct. Sci.* **1990**, *46*, 256–262. [[CrossRef](#)]
61. Bernstein, J.; Shimoni, L.; Davis, R.E.; Chang, N.-L. Graph set analysis of hydrogen-bond patterns in organic crystals. Recent developments and applications. *Acta Crystallogr. Sect. A Found. Crystallogr.* **1993**, *49*, c164. [[CrossRef](#)]
62. Grell, J.; Bernstein, J.; Tinhofer, G. Graph-set analysis of hydrogen-bond patterns: Some mathematical concepts. *Acta Crystallogr. Sect. B Struct. Sci.* **1999**, *55*, 1030–1043. [[CrossRef](#)]
63. Hirshfeld, F.L. Bonded-atom fragments for describing molecular charge densities. *Theor. Chem. Accounts* **1977**, *44*, 129–138. [[CrossRef](#)]
64. Spackman, M.A.; Jayatilaka, D. Hirshfeld surface analysis. *CrystEngComm* **2009**, *11*, 19–32. [[CrossRef](#)]
65. Turner, M.J.; McKinnon, J.J.; Wolff, S.K.; Grimwood, D.J.; Spackman, P.R.; Jayatilaka, D.; Spackman, M.A. *Crystal Explorer 17*; The University of Western Australia: Perth, Australia, 2017.
66. McKinnon, J.; Jayatilaka, D.; Spackman, M.A. Towards quantitative analysis of intermolecular interactions with Hirshfeld surfaces. *Chem. Commun.* **2007**, 3814–3816. [[CrossRef](#)] [[PubMed](#)]
67. Bellamy, L.; Owen, A. A simple relationship between the infra-red stretching frequencies and the hydrogen bond distances in crystals. *Spectrochim. Acta Part A Mol. Spectrosc.* **1969**, *25*, 329–333. [[CrossRef](#)]

68. Ignatyev, I.; Kondratenko, Y.; Fundamensky, V.; Kochina, T. Synthesis and characterization of cobalt(II) complexes with triethanolamine and succinate and/or nitrate anions. *Transit. Met. Chem.* **2017**, *43*, 127–136. [[CrossRef](#)]
69. Larabi, L.; Reguig, A.; Mostafa, M.; Harek, Y. Nickel(II) Complexes with Sulphonylhydrazone derivatives: Spectroscopic and electrochemical studies. *J. Appl. Sci.* **2008**, *8*, 3191–3198. [[CrossRef](#)]
70. Güveli, Ş.; Koca, A.; Özdemir, N.; Bal-Demirci, T.; Ülküseven, B. Electrochemistry and structural properties of new mixed ligand nickel(ii) complexes based on thiosemicarbazone. *New J. Chem.* **2014**, *38*, 5582–5589. [[CrossRef](#)]
71. Hamacher, C.; Hurkes, N.; Kaiser, A.; Klein, A.; Schüren, A. Electrochemistry and spectroscopy of organometallic terpyridine nickel complexes. *Inorg. Chem.* **2009**, *48*, 9947–9951. [[CrossRef](#)]
72. Safavi, A.; Fotouhia, L. Electrochemical oxidation of the Ni(II) complex of 2-amino cyclopentene-1-dithiocarboxylate at a Pt electrode. *J. Electroanal. Chem.* **1997**, *434*, 93–98. [[CrossRef](#)]



© 2020 by the authors. Licensee MDPI, Basel, Switzerland. This article is an open access article distributed under the terms and conditions of the Creative Commons Attribution (CC BY) license (<http://creativecommons.org/licenses/by/4.0/>).